

Achieving High Power Density and Durability of Sliding Mode Triboelectric Nanogenerator by Double Charge Supplement Strategy

Pengfei Chen, Yingjin Luo, Renwei Cheng, Sheng Shu, Jie An, Andy Berbille, Tao Jiang,* and Zhong Lin Wang*

Triboelectric nanogenerators (TENGs), a promising energy harvesting technology for distributed power sources, faces inevitable issues regarding long-term wear and durability. However, current low-wear TENGs are impaired by lower performances due to low charge density. Here, both issues are addressed using a double charge supplement TENG (DCS-TENG). Adding two low friction charge brushes allows the DCS-TENG to achieve a high surface charge density ($76.5 \mu\text{C m}^{-2}$) and power density ($697.5 \text{ mW m}^{-2} \text{ Hz}^{-1}$), setting a new record among previously reported low-wear TENGs. Moreover, the device exhibits unprecedented durability with an attenuation of only 5% after continuous operation for 110 h (3 960 000 cycles). Using a customized energy management module, a 3×7 hygrothermograph array, a high-power vehicle's radar and accelerometer modules are stably powered, demonstrating the DCS-TENG's strong electrical load capacity. This strategy provides a facile and effective path to conjointly boost power output and durability of TENGs, taking them to the next level for practical applications.

distributed energy supply toward present ubiquitous electronic devices.^[1] Therefore, innovation on energy supply systems to drive smart, widespread, and low-power sensors becomes an urgent matter.^[2] Triboelectric nanogenerators (TENGs, also called as Wang generator) have the potential to alleviate part of the problem of harvesting high entropy energy,^[3] for example, low-frequency environmental mechanical energy, using triboelectrification and electrostatic induction to produce the electric power for feeding electronics.^[4] They exhibit the advantages of light weight, low cost and versatile material choices, and have become a significant research direction.^[5] As such, TENGs have made remarkable progress in the fields of flexible wearable power supply,^[6] self-powered energy pack,^[7] high-voltage sources,^[8] blue energy,^[9] and so on.^[10]

1. Introduction

As the developments of Internet of Things (IoTs) and artificial intelligence progress, traditional “ordered” power supply methods encounter difficulties to meet the demand for a more

Generally, compared with the contact-separation mode TENG with instantaneous pulse signals, the sliding mode TENG (S-TENG), including freestanding (FS-) and lateral-sliding (LS-) modes, holds advantages of higher conversion efficiency,^[11] continuous and high average power for in-plane regular movement^[12] (e.g., reciprocation and rotation). They are currently considered as the best candidates for applications and commercialization, pushing the improvement of their output performance, especially the surface charge density, to the top of the priority list in this field. Various methods including charge shuttling,^[13] charge space-accumulation,^[14] design of micro-electrode unit,^[15] etc., have been proposed, leading to a charge density enhancement from 1.33 to 5.4 mC m^{-2} for the S-TENG. However, a large driving force is usually needed to drive the S-TENGs, resulting in inevitably large interface friction and consequential wear.

To reduce friction and improve service life time while preserving output performance, numerous research works on low-wear S-TENGs have provided several strategies, such as rolling friction,^[16] soft contact^[17] and non-contact.^[18] Our previous work reported a charge supplement method using an external tribo-material to form pseudo-non-contact TENG.^[19] This method minimizes frictional resistance while keeping a sustainable level of triboelectric charges. In addition, a floating self-excited FS-TENG has been proposed,^[20] using an amplifier circuit and

P. Chen, Y. Luo, R. Cheng, S. Shu, J. An, A. Berbille, T. Jiang, Z. L. Wang
CAS Center for Excellence in Nanoscience
Beijing Institute of Nanoenergy and Nanosystems
Chinese Academy of Sciences
Beijing 100083, P. R. China
E-mail: jiangtao@binn.cas.cn; zhong.wang@mse.gatech.edu

P. Chen, R. Cheng, S. Shu, J. An, A. Berbille, T. Jiang, Z. L. Wang
School of Nanoscience and Technology
University of Chinese Academy of Sciences
Beijing 100049, P. R. China

Y. Luo
School of Mechanical and Power Engineering
Chongqing University of Science & Technology
Chongqing 401331, P. R. China

Z. L. Wang
School of Material Science and Engineering
Georgia Institute of Technology
Atlanta, GA 30332-0245, USA

 The ORCID identification number(s) for the author(s) of this article can be found under <https://doi.org/10.1002/aenm.202201813>.

DOI: 10.1002/aenm.202201813

conductive slip rings, to address the charge decay issue inherent to this design. However, the low output power and weak electrical load capacity of present low-wear S-TENGs keep them away from practical applications. Developing an S-TENG with both strong durability and high output performance, while keeping the structure simple, is an essential but challenging task.

Herein, we propose a unique and simple design for LS-TENG benefiting from a double charge supplement strategy (DCS-TENG) that improves the performances of the device while keeping the friction wear low. The design of the DCS-TENG is applied to a traditional binary dielectric electrified layered system into which we introduce two other materials, namely positive and negative brushes, to form the quaternary dielectric triboelectrification. On the basis of an appropriate choice of materials, the charge brushes enhance the charge densities of the two main triboelectric layers. After optimizing the structural parameters of this system, its mechanism and performance were studied. The surface charge density of the DCS-TENG reaches $76.5 \mu\text{C m}^{-2}$. It is able to achieve a high power density of $6975 \text{ mW m}^{-2} \text{ Hz}^{-1}$, which is, for low-wear S-TENG, the highest reported value in the present literatures. Moreover, after 110 h of continuous operation (3 960 000 cycles), the attenuation observed is only 5%, demonstrating a high output stability. To demonstrate its potential for applications, a DCS-TENG device for vibration energy harvesting is utilized to directly power a 3×7 hygrothermograph array with the assistance of a customized energy management module. Finally, it is also applied to create a self-powered intelligent transportation system through powering radars and accelerometers in the vehicle continuously, verifying the DCS-TENG's strong electrical load capacity. The research presented here provides a facile and effective strategy for boosting the power output and durability of S-TENG and harvesting random ambient energy to provide a distributed energy supply.

2. Results and Discussion

2.1. Structure and Working Principle of DCS-TENG

Generally, the introduction of air gap is considered as an effective way to avoid mechanical friction and reduce the driving force between two tribo-layers in S-TENG. But, the disadvantages brought by the air gap can hardly be ignored. Mostly, it increases the probability for air breakdown to occur, limiting the output performance improvement.^[21] Take non-contact LS-TENG as an example to explain this phenomenon. Based on the equivalent physical model of the non-contact LS-TENG^[22] (Figure S1, Supporting Information), the capacitance of non-contact LS-TENG can be expressed by:

$$C = \frac{\epsilon_0 w(l-x)}{d_0} \quad (1)$$

where d_0 is the effective dielectric thickness and ϵ_0 represents the vacuum permittivity. Hence, the voltage of the air gap can be expressed by:

$$V_{\text{gap}} = \frac{Q}{C} = \frac{\sigma x d_0}{\epsilon_0(l-x)} \quad (2)$$

According to Paschen's law, the voltage that causes air breakdown between two parallel plates follows:

$$V_{a-b} = \frac{A(Pd_0)}{\ln(Pd_0) + B} \quad (3)$$

where P is the pressure of the gas, A and B are the constants determined by the composition and the pressure of the gas. For the air at standard atmospheric pressure of 101 kPa, A is $2.87 \times 10^5 \text{ V/atm m}$ and B is 12.6. So, to avoid the air breakdown effect, the V_{gap} needs to be smaller than V_{a-b} . Thus, there is a maximum charge density (σ_{max}) on the surface of the tribo-layers, which satisfies the following relation:

$$\sigma_{\text{max}} \leq \min\left(\frac{AP\epsilon_0}{\ln(Pd_0) + B} \left(\frac{l}{x} - 1\right)\right) \quad (4)$$

According to these equations, the maximum charge density of non-contact LS-TENG is greatly limited by the air gap d_0 , for a given lateral separation distance x . The detailed derivation process is documented in Note S1, Supporting Information.

Besides, numerous research results also proved that whether it is an LS-TENG or FS-TENG, the electrical outputs are very sensitive to the gap between the surfaces of two triboelectric layers.^[23] The charge transfer efficiency η_{CT} (defined as the ratio of the final short-circuit transferred charges to the total triboelectric charges) can be given by:^[23b]

$$\eta_{\text{CT}} = \frac{Q_{\text{SC,final}}}{\sigma S} = \frac{1}{1 + C_1(x = x_{\text{max}})/C_2(x = x_{\text{max}})} - \frac{1}{1 + C_1(x = x_0)/C_2(x = x_0)} \quad (5)$$

where σ and S are the surface charge density and surface area of the triboelectric layer, respectively. The detailed derivation process is recorded in Note S2, Supporting Information. The theoretical analysis shows that an increase of air gap engenders a great decrease of charge transfer efficiency, which has been herein verified experimentally as well. Besides, the outputs of LS-TENGs are more susceptible to the gap between the surfaces of two triboelectric layers than FS-TENG,^[23a] but strategies to promote the output performance of non-contact LS-TENG are rarely proposed and no breakthrough has been made since 2013. To put it briefly, there seems to be a contradiction between low wear and high performance characteristics of TENGs. Indeed, the presence of an air gap reduces wear and improves durability, but the consequential air breakdown and significant reduction in charge transfer efficiency make it difficult to improve their performance.

The newly designed LS-TENG herein achieves double charge supplement by the utilization of additional triboelectric materials as charge brushes. **Figure 1a** illustrates the device structure. Here, polytetrafluoroethylene (PTFE) and polyethylene terephthalate (PET) films were used as tribo-materials of a traditional binary system. To reduce contact friction and wear, the two tribo-materials are separated by a fixed distance (air gap) forming a non-contact part structure. The cross-section schematic of the stationary part and sliding part is depicted in

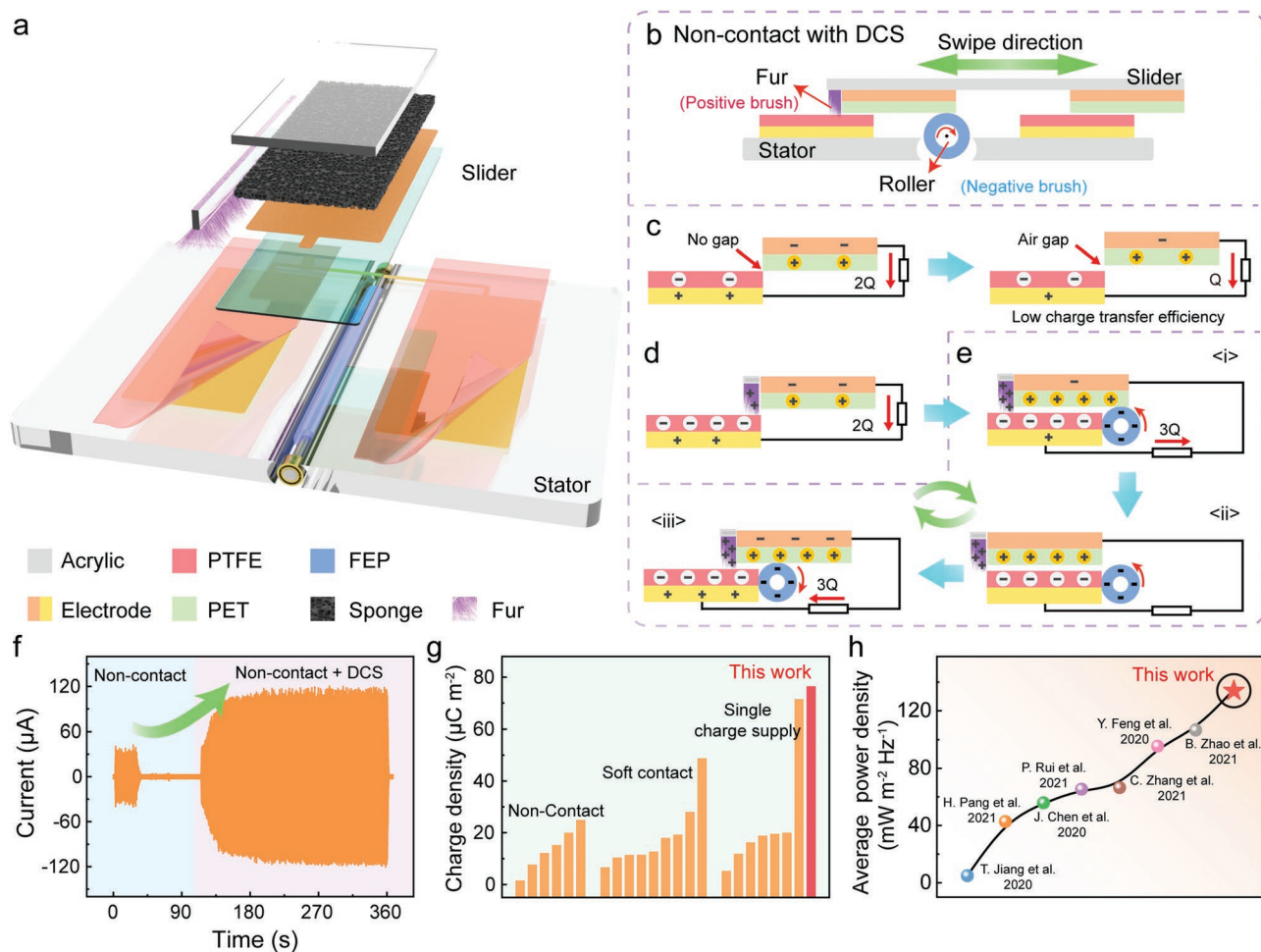


Figure 1. Structure and working principle of the DCS-TENG. a) 3D structural schematic of the DCS-TENG unit. b) Cross-section view showing the configuration of each part of the non-contact TENG with double charge supplement. c) Schematic working mechanism of traditional non-contact sliding-TENG. d) Schematic diagram of the TENG with single charge supplement. e) Working mechanism and charge distribution states of the DCS-TENG in three states during a working period. f) Dynamic output current curves under two working circumstances, showing the powerful output boosting ability of our designed DCS-TENG. g) Comparison of the charge density of DCS-TENG with different types of low-wear TENGs. h) Comparison of the average output power density of this work with that reported by others.

Figure 1b. However, the charge transfer efficiency between two tribo-layers is lower in the non-contact mode, compared to the contact-mode S-TENG, as shown in Figure 1c. In addition, the quick decay of pre-existing charges on both triboelectric layers also results in a continuous drop in electric outputs during prolonged operation.

In order to compensate for these hindrances, we introduce two charge supplementing materials, namely positive and negative brushes, to the binary system. This modification's purpose is to increase the surface charge density of the tribo-layers, thus maintaining the triboelectric charges on the material surfaces during operation. Owing to their elasticity, softness and excellent triboelectric property, rabbit fur brushes were chosen as the positive triboelectric supplementary material. Its ability to provide tight contact while keeping a low friction state, results in more triboelectric charges gained for the PTFE film from the rabbit fur, causing an increase in the amount of transferred charges, as shown in Figure 1d. Similarly, adding fluorinated ethylene propylene (FEP) rollers as the

negative triboelectric supplementary material provides a further improvement of the TENG output. It is worth mentioning that the coefficient of friction between rabbit fur and PTFE/FEP is extremely small, and almost negligible. Moreover, the rabbit fur has extremely high hair density. The nano-diameter hair fibers effectively increase the effective contact area, thereby the higher triboelectric charge density can be achieved during the friction. The working mechanism and charge distribution states of S-TENG with double charge supplement, in three states during a working period, are illustrated in Figure 1e. In the initial state (state i), due to the presence of rabbit fur and FEP roller, higher surface charge densities are obtained for both tribo-layers. And when the slider reciprocates relative to the stator, the alternating current is generated between the electrode pairs through an external circuit due to electrostatic induction (states i–iii). The amount of charge transfer is greatly increased, compared with traditional non-contact mode S-TENG. The detailed fabrication process of the device is presented in the Experimental section.

Figure 1f shows the dynamic output current curves under two working circumstances, showing the considerable output boosting ability of our designed DCS-TENG (more details are shown in Figure S2 and Video S1, Supporting Information). The charge supplementing effect can be observed and the charge output reaches a stable state quickly, once the charge brushes are added. Figure 1g shows a comparison of charge density generated by the DCS-TENG and the other three low-wear sliding TENGs presented in recent research articles, including: 1) the normal non-contact TENG; 2) soft-contact TENG with material selection; and 3) non-contact TENG with single charge supplement. After optimizing the structure of the device, the DCS-TENG attains a stable output charge density of $76.5 \mu\text{C m}^{-2}$, at an air gap of 0.35 mm, and the maximum peak and average power densities reach 697.5 and $135.0 \text{ mW m}^{-2} \text{ Hz}^{-1}$. These are currently higher than the values reported in previous researches on low-wear S-TENGs (Figure 1h, and Figures S3 and S4 and Table S1, Supporting Information). Such

a high output power makes it possible for the TENG to drive some high-power devices like vehicle radar, taking TENGs to a new level when it comes to practical applications.

2.2. Optimization of Structural Parameters

To investigate the influences of structures and materials on the DCS-TENG deeply, we created a standard measuring system capable of controlling precisely the gap between two tribolayers, as illustrated in Figure 2a. The set-up contains a support for the slider, and a XYZ-R stage for the stator. A height-adjustable high-load lab jack supports a linear motor, permitting fine adjustments of the height and horizontal positions of the slider. The stator is mounted on a three-axis rotating stage (Figure S5, Supporting Information), that enables the adjustment of the plane parallelism of the stator and the slider by rotation, and controls the gap size between them with an accuracy of

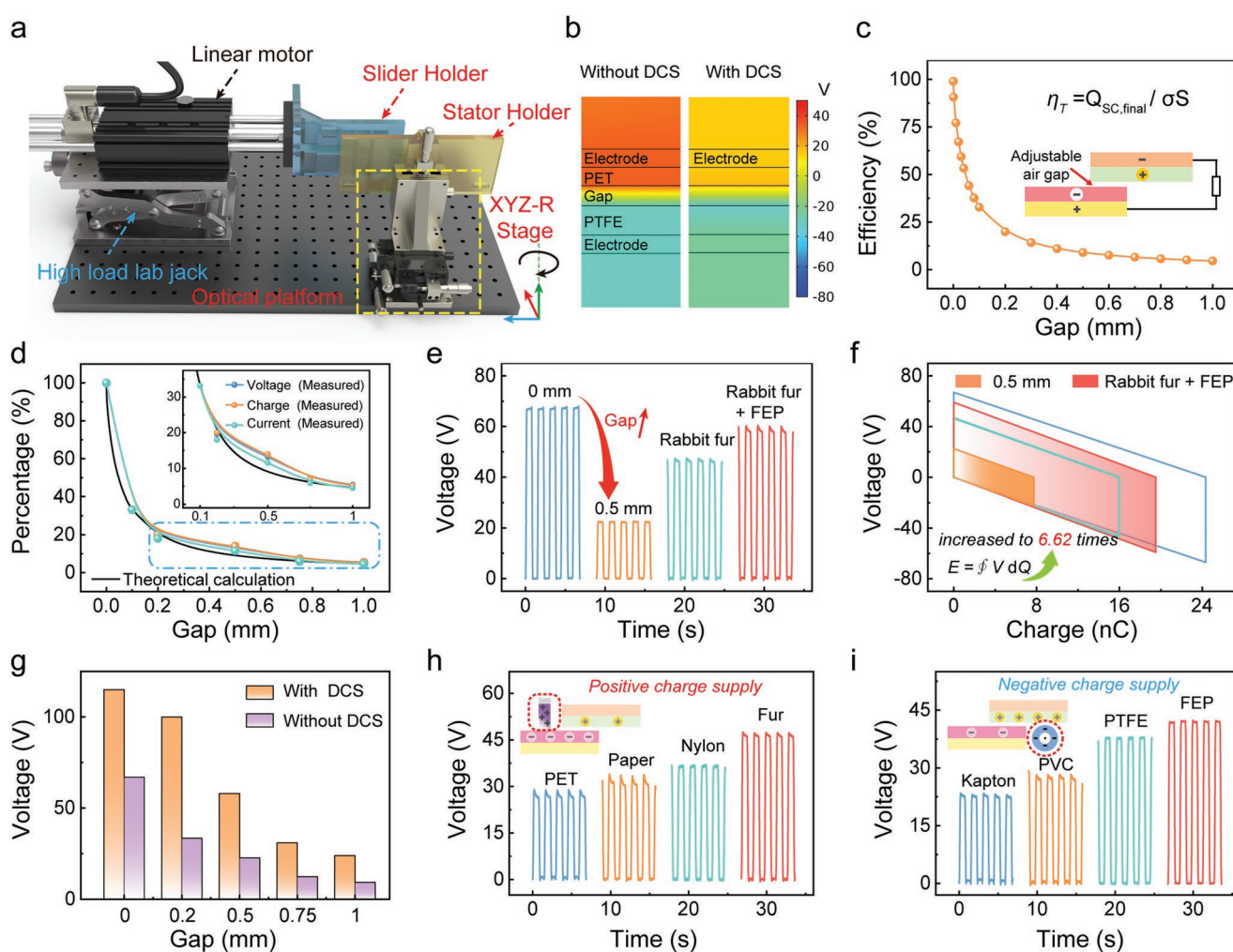


Figure 2. Mechanism and material selection of the DCS-TENG unit. a) 3D schematic of experimental set-up for the double charge supplement strategy. b) Potential simulations of the TENGs with/without DCS. c) The effect of air gap size on the charge transfer efficiency of sliding-mode TENG. d) The plots of experimental and theoretical outputs versus the gap for the non-contact TENG, demonstrating the reliability of our experiments. e, f) Voltage output and $U-Q$ plots of TENGs under four different working conditions. g) Output comparison with/without the DCS at different air gaps. Output voltage of sliding-mode TENG with fixed triboelectric materials while h) varying positive charge supplement materials, and i) varying negative charge supplement materials.

0.01 mm. Figure 2b shows the electric potential distributions in the air gap between two tribo-layers, with and without the charge supplementing materials. The simulation indicates that for a given surface charge density of the tribo-layers, the presence of the charge brush significantly reduces the potential difference in the air gap (Figure S6, Supporting Information). And the higher the charge density of the charge brush, the lower the potential difference in the air gap, allowing the triboelectric material to achieve greater surface charge density. This is crucial for improving the output performance.

The effect of air gap on the charge transfer efficiency for LS-TENGs is indicated in Figure 2c. It appears that the air gap tolerance of sliding-mode TENGs is poor. Indeed, the charge transfer efficiency will decay exponentially as the air gap increases. This is also demonstrated by the experimental data presented in Figure 2d. In the experiments, a standard feeler gauge was used to settle the initial air gap between the stator and the slider at 0.1 mm. And a gap of 0 mm can be obtained by adjusting the high-precision stage. Then, we measured the outputs of the TENGs with varying air gaps. Since the effective contact area of the tribo-layers can only reach $\approx 6.16\%$ in actual experiments,^[21] we calculated the theoretical output of TENG assuming an effective contact area of 100%, that is in intimate contact state (0 mm), by applying the simulated charge transfer efficiency obtained at the gap of 0.1 mm (Figure 2d). The experimental results show that, whether we examine output voltage, current or transferred charge, the experimental and theoretical output trends are in good agreement at different gap values. It confirms that the air gap is indeed a critical factor to determine the amount of charge transfer and proves the reliability of our experimental setup.

According to above theoretical analysis and experimental results, a series of experiments were carried out for further investigations on the influences of structures and materials on the DCS-TENG. Here, we used PET and Kapton (PI) films as the two tribo-layers, and tested the peak voltage output of S-TENG. First, according to the positioning method, the initial state (0 mm) is obtained by fine-tuning the XYZ platform from the 0.1 mm gap. When the gap is increased to 0.5 mm, the open-circuit voltage drops from 67 to 22.8 V, with an attenuation of more than 50%. Then, by successively adding the rabbit fur and FEP films, the output is significantly improved to 58 V at the gap of 0.5 mm, a 2.54-fold enhancement, as shown in Figure 2e. The $U-Q$ curves of TENGs under four different working conditions are plotted in Figure 2f. Contrasting the energy outputs indicates that the energy harvested is increased to 6.62 times after adding two low friction charge brushes at a 0.5 mm gap. As we can see in Figure 2g, the TENG outputs with the DCS are all higher than those without DCS, demonstrating the effectiveness of double charge supplement strategy to boosting the performance regardless of the gap.

Second, we systematically measured the outputs of DCS-TENG for given triboelectric materials while varying the signs of the charge supplement materials. It should be noted in each experiment, the tribo-layers between the slider and the stator are pre-contacted and triboelectrically charged until full saturation at a 0 mm gap (Figure S7, Supporting Information). The gap is, then, adjusted to 0.5 mm to explore the effect of different charge supplementary materials, which fully guarantees

the consistency of the experiment. We can see that when PET is used as a supplementary material, there is only a slight improvement in the performance (Figure 2h). This is because the surface charge density of PI is already a saturated value obtained by intimate contact friction with PET. Therefore, the PI should not be able to obtain more triboelectric charges from the PET. But, due to the presence of supplementary materials, the potential difference between the two tribo-layers is reduced, allowing the tribo-layer to hold more charges, which results in slightly-improved output performance. So, higher output can be achieved by using more positive triboelectric material, such as rabbit fur, because the PI film obtains more triboelectric charges from the charge brush. Correspondingly, the maximum output can also be obtained by using FEP as a negatively charged brush as seen in Figure 2i.

2.3. Output Performance and Durability of Arrayed DCS-TENG

The above studies demonstrated the excellent performance-enhancing ability of the charge supplement strategy. Therefore, we fabricated arrayed DCS-TENGs with different electrode widths for better energy harvesting. Figure 3a shows the output charge density of the arrayed DCS-TENG with an electrode width of 6.7 mm under four working conditions. After introducing FEP and rabbit fur as the charge supplement materials, the charge density reaches $65 \mu\text{C m}^{-2}$ at the gap of 0.5 mm, and $76.5 \mu\text{C m}^{-2}$ at the gap of 0.35 mm, thus setting a new record for non-contact S-TENG (Figure S3 and Table S1, Supporting Information). Moreover, the excellent performance-enhancing ability of the charge brush for the non-contact S-TENG are still observable for varying electrode widths, as illustrated in Figure 3b–d. As the electrode width decreases, the effective charge density increases significantly when sliding the same distance, reaching up to 0.5 mC m^{-2} for a width of 4 mm. The short-circuit current can also be increased up to 16 μA . And as analyzed above, the maximum surface charge density of the tribo-layer depends on the triboelectric material and its triboelectricity, and is limited by air breakdown at the same time. Therefore, the number of rabbit fur and FEP rollers may only affect the relaxation time for the device to reach stable output due to the larger contact area, but not its maximum stable output performance.

Now, we define the replenishment efficiency as the ratio of the DCS-TENG output to the TENG output without DCS, for a 0.5 mm air gap. For different electrode widths, the replenishment efficiencies for the output voltage and charge both reach around 180%. It is worth noting the measured outputs are close to those observed at intimate contact state (above 80%, Figure S8, Supporting Information). And the output current can still be further improved by increasing the driving frequency, attaining 30 μA at only 1.5 Hz (Figure 3e). Note that the current output of the device shows the form of pulse peak packets, which is because the motion mode of the slider is a quasi-simple harmonic motion and the output current is obtained by dQ/dt . The acceleration and deceleration time of the slider cannot be ignored in the reciprocating motion. A stable output can be obtained by selecting a rotating TENG structure capable of uniform motion for harvesting energy of rotational motion,

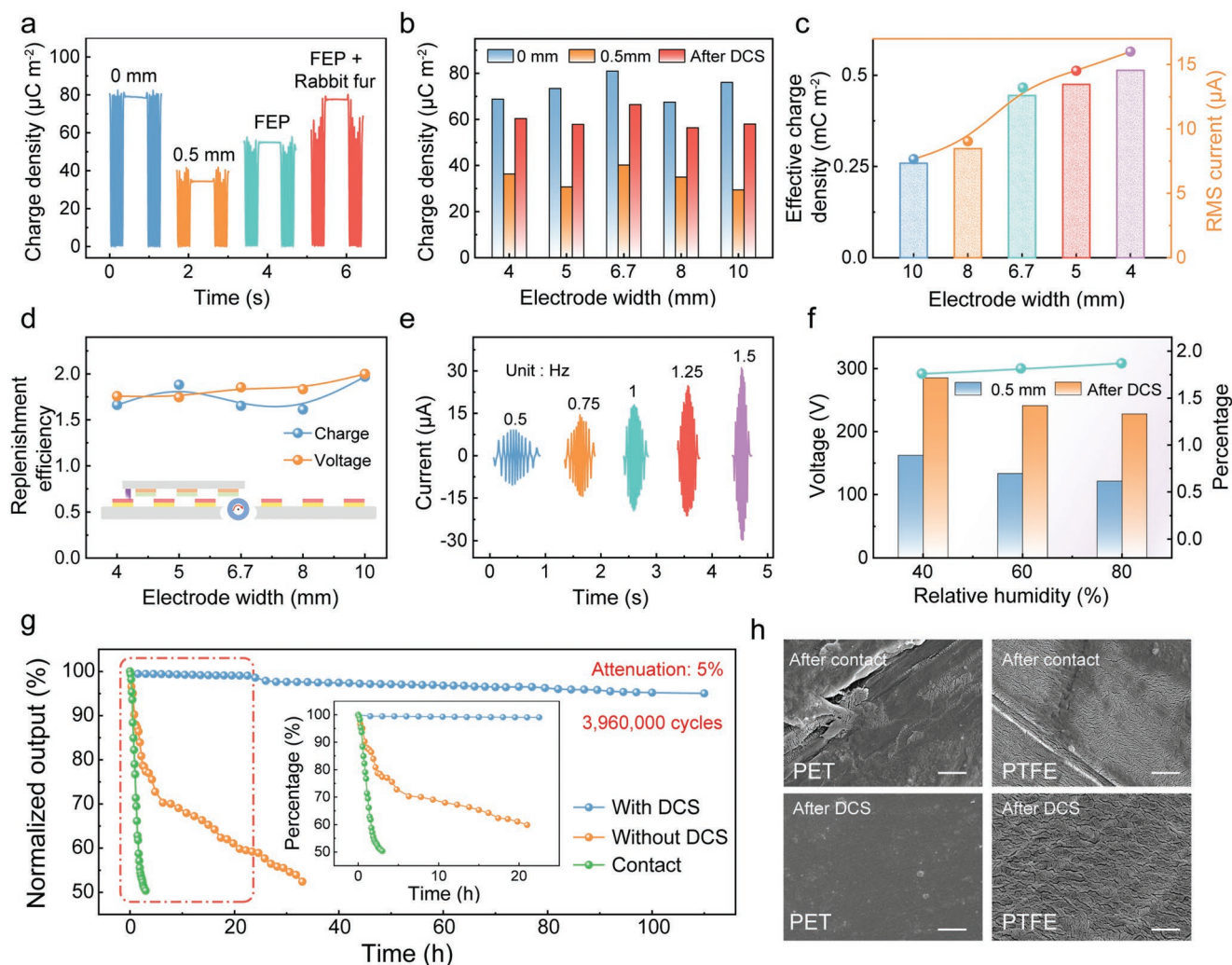


Figure 3. Output performance and durability of the arrayed DCS-TENG. a) Output charge density of the arrayed DCS-TENG with an electrode width of 6.7 mm under four working conditions. b) Output charge density of the arrayed DCS-TENGs with different electrode widths. c) Effective charge density and current output of the DCS-TENGs with different electrode widths after double charge supplement. d) Performance replenishment efficiency of DCS for the non-contact TENGs with different electrode widths. e) Current outputs of the DCS-TENG at various driving frequencies. f) Influence of environment humidity on the DCS-TENG output and replenishment efficiency. g) Long-term durability testing over 100 h for the non-contact mode with or without DCS and contact mode. h) Comparison of the material abrasion for two modes of TENGs after 50 h of continuous testing (scale: 2 μm).

like our previous work.^[5a] Thereafter, the effect of ambient humidity on the charge supplement was also studied as in Figure 3f. As the humidity increases, the transferred charge decreases due to the difficulty in stabilizing the surface charges at high humidity. However, it can also be seen that the charge brushes retain excellent charge supplementing ability at any relative-humidity. More interestingly, the charge replenishment efficiency is higher under high humidity, which can reach 190%, than that under low humidity. This result shows the applicability of charge supplement from charge brushes in various working conditions.

Besides, the introduction of the charge brushes effectively solves the performance attenuation problem of non-contact S-TENG, due to the quick decay of surface charges. We propose that the charge brushes are capable of replenishing the surface charges, that are normally decaying, as they slide on the tribo-surfaces of the DCS-TENG. The long-term durability test

results of the DCS-TENG are shown in Figure 3g. The normalized current of the S-TENG with the DCS indicates a tremendous electrical stability compared with that of the contact or non-contact TENG (without the DCS). The DCS-TENG maintains 95% of the initial output after 110 h (3 960 000 cycles). However, the performance of both non-contact and contact TENGs without the DCS declines by more than 50% after 35 and 3 h, respectively. In addition, a standardized metric of durability is proposed, which is the rate of the number of cycles and the decay rate, as shown in Figure S9, Supporting Information, to compare with other works. It demonstrates the unprecedented advantage of double charge supplement strategy, with a 2.85-fold increase in the durability compared to a previous work. Furthermore, observations by scanning electron microscopy (SEM) show the extent of material abrasion after 50 h of continuous testing (Figure 3h and Figure S10, Supporting Information). The mechanical wear of DCS-TENG is negligible

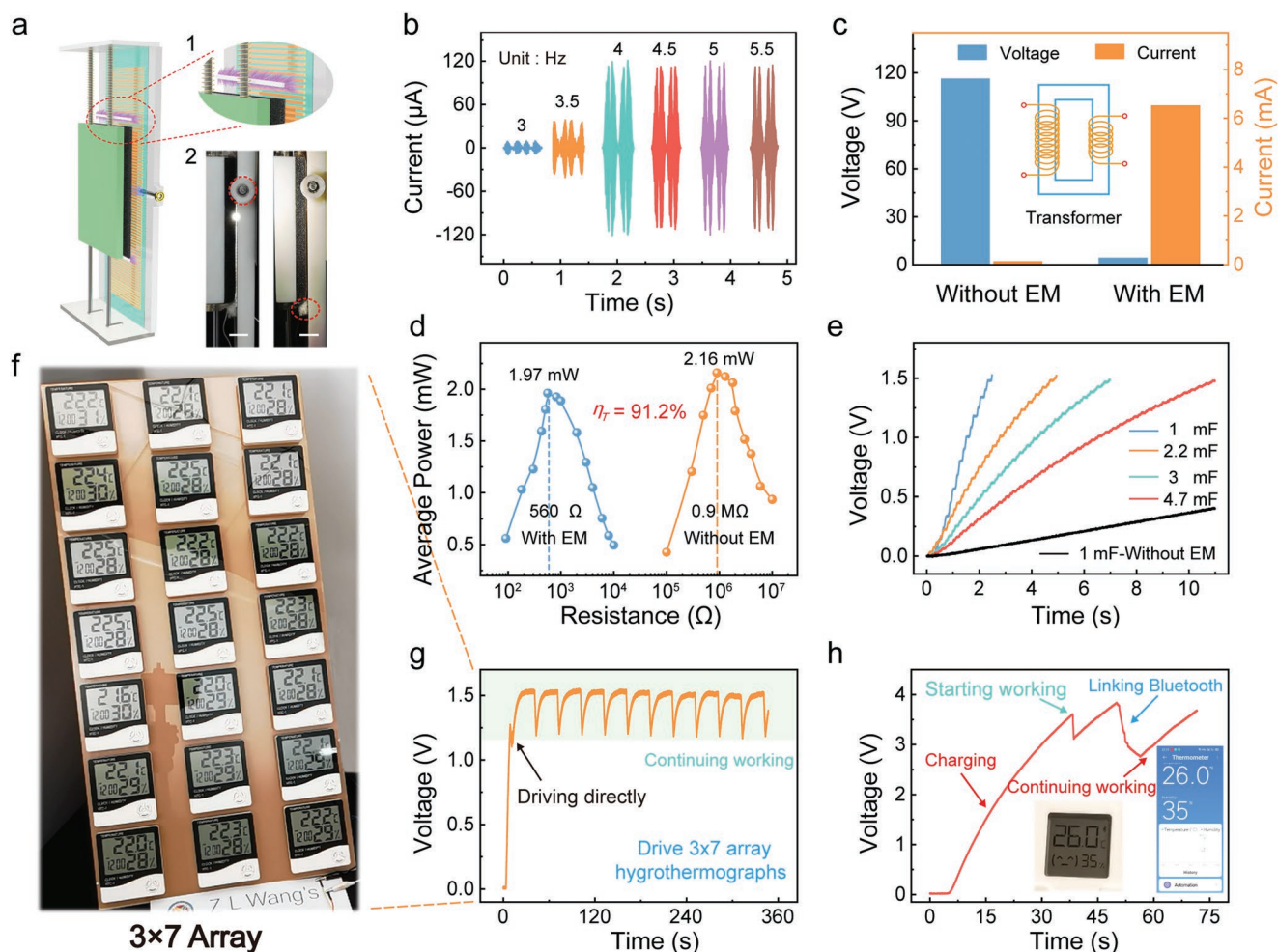


Figure 4. Performance and application of the DCS-TENG devices for vibration energy harvesting (DCS-V-TENG). a) The 3D schematic of the DCS-V-TENG device. Inset 1: locally enlarged schematic diagram of the charge supplement structure. Inset 2: photographs of key parts of the device, including clearly visible air gaps, FEP roller and rabbit furs. Scale bar: 1 cm. b) Output current of the DCS-V-TENG with different vibration frequencies at fixed vibration amplitude of 25 mm. c) Comparison of the output voltage and current of the DCS-TENG with and without energy management (EM). d) Comparison of average output power between the cases with and without the EM unit. e) Voltage curves on various charging capacitors at fixed vibration frequency of 4 Hz and amplitude of 25 mm. f) Actual image of the 3×7 arrayed hydrothermographs driven directly by the DCS-V-TENG with the EM unit. g) Voltage of the hydrothermograph array in parallel driven by the DCS-V-TENG. h) Voltage of the wireless Bluetooth sensor which are continually driven by the DCS-V-TENG with the EM unit.

compared to that of contact mode TENG, except for some debris and rolling marks from the rabbit furs and rollers. In summary, the DCS-TENG not only generates a high electrical output, but also exhibits excellent long-term durability compared with that of classical contact-mode TENG.

2.4. Performance and Application of DCS-TENG Devices for Vibration Energy Harvesting

As one of the most prevalent forms of energy source in the surrounding environment, mechanical vibrations have great potential as a power source for self-powered electronics. A vibration energy harvesting device based on the TENG with double charge supplement strategy (DCS-V-TENG) was fabricated. In order to simplify the manufacturing process and achieve higher outputs, an array of flexible copper electrodes with a width of

1 mm was fabricated by the printed circuit board (PCB) technology. It is used as a positive triboelectric material for the slider in the device, in place of the previously employed PET film. Rabbit fur brushes and FEP rollers are still used as the charge supplementary materials. Two springs and two sliding bars support the slider and ensure that it moves only in the direction of the vibration, as shown in **Figure 4a**. By adjusting the position of the slider bars, we can precisely tune the gap between the slider and the stator using a feeler gauge. The insets 1 and 2 depict the details of the device, and we can clearly see the gaps through which the rear light source travels easily. The red marked positions represent the two charge brushes we installed. The slow-motion footage of the device in actual motion can be seen in Video S2, Supporting Information. The device can be simplified to a single degree-of-freedom damped free vibration model, and the natural frequency will be determined by part parameters such as the stiffness coefficient of

the spring, the length and the mass of the slider. The detailed derivation process can be seen in Note S3, Supporting Information. The natural frequency of the device can be changed as required by adjusting the part parameters.

Figure 4b displays the output current of the DCS-V-TENG with different vibration frequencies at fixed vibration amplitude of 25 mm. When the vibration frequency reaches 4 Hz, the short-circuit current of the DCS-V-TENG exceeds 110 μA . At such a low-frequency and small-amplitude range (<5 Hz), the TENG has incomparable advantages over the electromagnetic generator (EMG). As demonstrated in Figure S11 and Video S3, Supporting Information, 300 high-power LEDs with a diameter of 10 mm are easily powered and shine brightly. To further improve the performance and match the requirements of electronics, a customized energy management (EM) circuit was added. The EM circuit lowers the output voltage, and concomitantly enhances the current output from the DCS-V-TENG, as shown in Figure 4c. The operating frequency of this customized transformer was set to be 30 Hz. At a vibration frequency of 4 Hz, the maximum peak value of the short-circuit current after the transformer rises from 110 μA to 6.5 mA, while the output voltage drops from 115 to 4 V. The peak and average output power of the DCS-V-TENG with or without EM with respect to the load resistance was plotted as in Figure 4d and Figure S12, Supporting Information. The blue curve shows the average output power through the EM, with a load resistance varying from 0.01 to 10 k Ω , reaching a maximum of 1.97 mW at 560 Ω . Without the EM, the maximized average output power is 2.16 mW, for a load resistance at 0.9 M Ω . An overall energy conversion efficiency of 91.2% is achieved using our EM, which is much higher than that of previously reported energy management strategies.^[24] Utilizing an effective area of 40 cm², the peak and average power density with EM can be as high as 650.0 and 123.1 mW m⁻² Hz⁻¹, respectively. It is worth noting that the matching impedance of maximum power output is brought from 0.9 M Ω down to 560 Ω , a reduction of more than 1600 times that is essential for practical applications of TENG. With the support of the EM, a 1 mF capacitor is charged to 1.5 V within 2.4 s, and only up to 0.08 V without the EM (Figure 4e). The accumulation of energy in the capacitor over time is plotted in Figure 11c, Supporting Information. Over 5 mJ of energy can be easily stored \approx 10 s with the assistance of the EM, providing a 58-fold improvement in energy extraction capacity.

Owing to the high outputs and extremely low matching impedance of the DCS-V-TENG assisted by the EM circuit, some high-power applications, such as driving commercial hygrothermograph array and wireless Bluetooth, can be carried out. Figure 4f and Video S4, Supporting Information, display the actual image of a paralleled 3×7 hygrothermograph array that was driven directly to work continuously and stably, by the DCS-V-TENG/EM ensemble. The real-time working voltage curve of the hygro-thermometer array is presented in Figure 4g. Our DCS-V-TENG directly charges the 1 mF capacitor from 0 V to the working voltage and keeps it, showing its strong electrical load capacity. Figure 4h presents the working voltage plot on the wireless Bluetooth transmission module. The signals are wirelessly transmitted to a mobile phone successfully, as demonstrated in Video S5, Supporting Information. These applications powerfully demonstrate the unprecedented performance

of our system comprising the DCS-V-TENG with the EM unit, greatly accelerating the extensive applications of TENGs for self-powered sensor networks and high-power devices for the IoTs.

2.5. Application of DCS-V-TENG in Smart Transportation

With the rapid development of the mobile internet and industry 4.0, the Internet of Vehicles centered around intelligent connected vehicles (ICVs) is gradually entering people's lives. With the help of environmental perception system supported by a large number of intelligent devices, such as radars, cameras, sensors, etc., these vehicles can perceive and analyze environment to take decisions, which could significantly reduce the occurrence of vehicle rear-end collisions, traffic jams, thus improving the comfort and security of travelers (Figure 5a). However, the environmental impact of the widespread use of batteries powering this huge information network is a problem that must be considered. A possible solution for vehicles is to make each device self-powered by harvesting the vibrational energy produced during the vehicles' operation using TENGs. Here, to take advantage of the excellent output performance of our manufactured DCS-V-TENG, we install it on the shock absorber of the vehicle to collect vibration energy. The device steadily powers the radar and accelerometer modules, as illustrated in Figure 5b. Radars in automobiles perform a series of functions, such as speed measurement, ranging, blind spot detection, etc., that plays a vital role in vehicle active safety, intelligent assisted driving, and even unmanned driving. The accelerometer is also an important sensor which measures the instantaneous acceleration and direction, providing functions of collision warning and recording of driving patterns.

By harvesting the energy produced by the vibrations of the vehicle while driving, using the DCS-V-TENG, a self-powered intelligent wireless warning system is established (Figure 5c). The signals from the radar and accelerometer are wirelessly transferred to a terminal, such as smart phones, laptops or external servers, through WiFi modules and Cloud Server. It is worth mentioning that, the Cloud Server has the ability of multi-client access, and uploading the driving data of the car to the cloud server greatly facilitates the construction of the Internet of Vehicles. In order to simulate a practical scenario, we constructed a similar road environment, thus demonstrating the electrical load capacity of the DCS-V-TENG, as shown in Figure 5d. In the experiments, radar probes and accelerometers are installed on the front part of the simulated car. They are able to detect the distance between the car and the obstacle in front and measure the actual acceleration in real time (Video S6, Supporting Information). A LabView program was developed to acquire and process the signals from the WiFi module and realize the self-powered warning. The program interface is exhibited in Figure S13, Supporting Information, which displays the acquired instantaneous accelerations of XYZ axis, the angle with the positive direction of X axis, as well as the distance to the obstacle ahead in real time. The processing method of acceleration data is described in Note S4, Supporting Information. The system we built can not only issue safety warnings when the distance between obstacles is

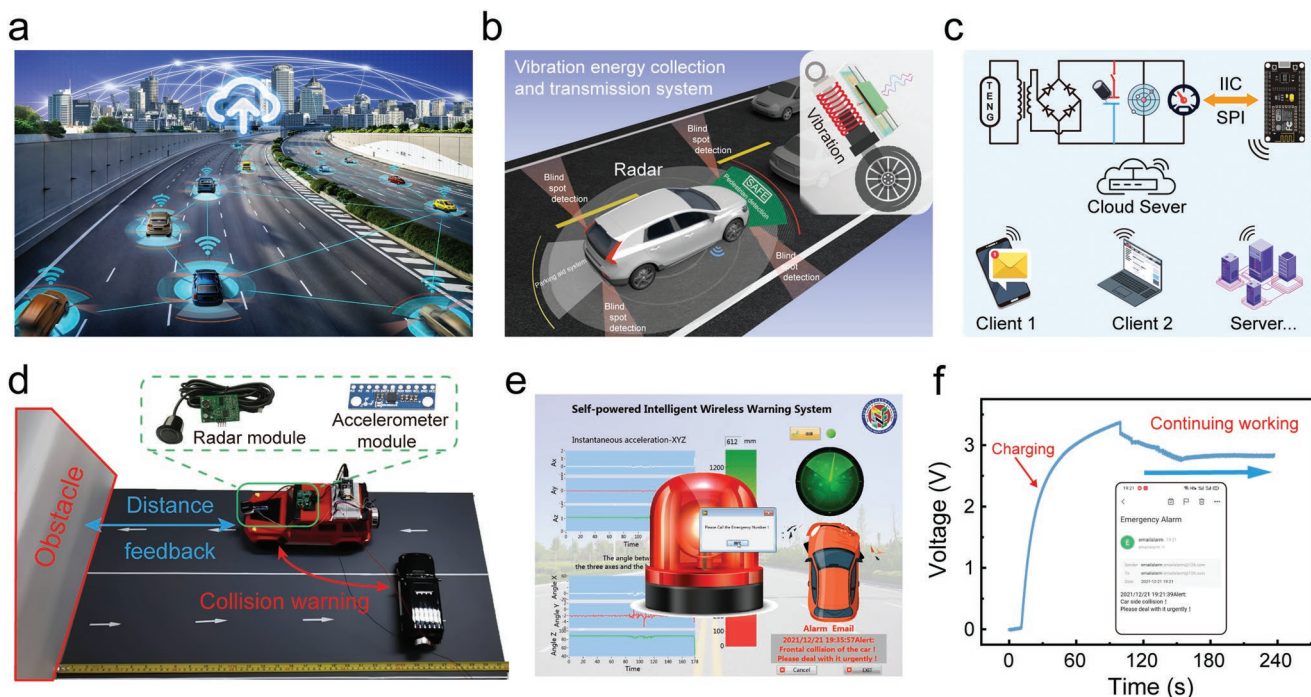


Figure 5. Application of the DCS-V-TENG in smart transportation. a) Proposed concept of applying the DCS-V-TENG in Internet of Vehicles. b) Scene graph of vibration energy harvesting and transmission system based on the radar powered by the DCS-V-TENG. c) Schematic diagram of circuit connection and wireless data transmission system. d) Demonstration of self-powered smart transportation. e) Wireless terminal display interface of self-powered intelligent wireless warning system, showing the alarm interface when the frontal collision of the car occurs. f) Voltage profile on the capacitor to power the radar and accelerometer modules, which can continue working stably. The inset is a screenshot of the alarm email when the car has a side collision.

less than the safe distance, but it is also able to judge collisions from different directions, ring an alarm and send out email alerts for timely rescue. Videos S7 and S8 and Figures S14–S16, Supporting Information, show the interaction between the terminal and the actual vehicle, and include cases of frontal and side collisions. Figure 5e shows the alarm interface of the terminal system when the frontal collision of the car occurs. The voltage curve of the capacitor to power the radar and accelerometer modules is plotted in Figure 5f, and Figures S17 and S18, Supporting Information. The voltage of the capacitor remains stable and continuously supplies power for the sensors, proving the stability allowing our self-powered system based on the DCS-V-TENG to operate in such conditions.

3. Conclusion

In summary, we have constructed a high-performance non-contact LS-TENG based on the double charge supplement strategy, which exhibits merits of both low wear and high output performance. The introduction of the charge brushes effectively reduces the potential difference between the two tribo-layers to achieve a high surface charge density of $76.5 \mu\text{C m}^{-2}$, which is a new record in low wear non-contact S-TENG. Moreover, after 110 h (3 960 000 cycles) of stability testing, the DCS-TENG exhibits excellent durability with an attenuation of only 5%. With appropriate energy management, a 3×7 hygrothermograph array can be directly powered by the DCS-TENG with a

record average power density of $135.0 \text{ mW m}^{-2} \text{ Hz}^{-1}$ while harvesting a low frequency vibration energy of 4 Hz. Finally, a self-powered intelligent transportation system based on radar and accelerometers was proposed, which operates stably, demonstrating the powerful output of such TENG. This work provides a promising strategy and strong proof of concept for long-term applications of TENG as distributed energy sources for the Internet of Things.

4. Experimental Section

Fabrication of the DCS-TENG Unit: Stator: i) a square acrylic sheet with a side length of 60 mm as the substrate was cut employing a laser cutter (PLS6.75); ii) a Cu electrode of $15 \text{ mm} \times 35 \text{ mm} \times 35 \mu\text{m}$ with a chamfer of 1 mm was adhered to the middle of the surface on the substrate; and iii) a $50 \mu\text{m}$ -thick Kapton film with the same dimension as the Cu electrode was attached to the upper surface of the Cu electrode as the negative triboelectric layer. Slider: i) a rectangle acrylic sheet with the dimension of $15 \text{ mm} \times 35 \text{ mm} \times 5 \text{ mm}$, used as the substrate, was cut using a laser cutter; ii) a conductive tape of the same size as the stator's Cu electrode was glued to the acrylic substrate, acting as the slider's electrode; and iii) a PET film with the dimension of $15 \text{ mm} \times 45 \text{ mm} \times 50 \mu\text{m}$ was attached to the overall surface of the conductive tape and the side of acrylic substrate to prevent edge warping. Different kinds of charge brushes were purchased directly from the market. Through manual contact friction, the charge density of the tribo-layer was increased to varying degrees to explore the charge supplement ability of different materials. The Cu electrodes of both the stator and the slider were connected through wires for electrical measurements. The

stator and the slider were respectively fixed on their respective supports using the designated slots.

Fabrication of the Arrayed DCS-TENG: The slider comprises a rectangle acrylic sheet with a dimension of 8 cm (length) by 6 cm (width) by 5 mm, used as the substrate, that was cut by a laser cutter. For each structural unit of the slider, conductive tapes with different widths were used as electrodes and attached to a 1 mm-thick sponge that was glued to an acrylic substrate for improving the material contact. Taking 6.7 mm-wide electrodes as an example, the number of electrodes is 6, and each electrode is 50 mm-long and 6.7 mm-wide. Note that when varying the electrode width, the total effective electrode area (20 cm²) remains the same. Then, the PET film with a dimension of 6.7 mm by 50 mm by 50 μm was attached to the overall surface of the conductive tape electrodes, as a positive triboelectric material. In accordance with the test results, rabbit fur was selected as the positive charge supplement material. So, the rabbit fur brushes of 50 mm in length and 3 mm in width were glued to both sides of the acrylic substrate.

For the stator, a substrate with a dimension of 18 cm (length) by 7 cm (width) by 10 mm, with a through hole in the center, was 3D printed. The central hole was used to mount the optical shaft and bearing. Through experimental tests, the hollow FEP tube was selected as the negative charge supplement material mounted on the optical axis. The installed FEP tube was placed at ≈0.5 mm above the top surface of substrate to contact the tribo-layer of slider for supplying charges. Flexible copper films with different numbers and width of electrodes prepared by the printed circuit board (PCB) technology were adhered to the substrate. The central part of the copper film is hollowed out to accommodate the raised part of the FEP tube. Then, the 80 μm-thick PTFE film was attached to the copper electrode as the triboelectric layer.

Fabrication of the DCS-V-TENG: The installation method of the two charge brushes (FEP roller and rabbit fur) is the same as that of the arrayed DCS-TENG. The difference is that the electrode width of the stator and slider of DCS-V-TENG is 1 mm. In detail, for the stator, first, the 80 μm-thick PTFE film was attached to the entire surface of the stator. After that, the excess PTFE film on the non-electrode part of the stator was cut off using a low-power laser cutter. Two acrylic plates with adjustable mounting holes were mounted on both ends of the stator substrate for fixing the slide bars and springs. For the slider, the flexible copper electrode array with a width of 1 mm replaced the previous PET film as the positive friction material. The substrate with a dimension of 9 cm (length) by 6 cm (width) by 10 mm with two through holes was 3D printed. Four linear bearings with an inner diameter of 3 mm were mounted on both ends of the through holes. Two springs and two sliding bars were used to support the slider and ensure that the slider moves only in the vibration direction. The gap between the stator and slider was determined using a feeler gauge.

Electrical Measurement and Characterization: All devices were fixed on an optical platform for measurements. The sliding motion was conducted using a linear motor (TSMV120-1S). The short-circuit current, transferred charges, and open-circuit voltage were measured by an electrometer (Keithley 6517). The humidity of the chamber can be intelligently controlled by a commercial humidifier and stabilized around a certain set value. The room temperature (15–25 °C) and humidity (20–85% RH) were measured by a commercial hygro-thermometer.

Supporting Information

Supporting Information is available from the Wiley Online Library or from the author.

Acknowledgements

P.C. and Y.L. contributed equally to this work. This work was supported by the National Key R & D Project from Minister of Science and Technology (2021YFA1201603, 2021YFA1201601), the National Natural

Science Foundation of China (Grant No.51432005, 51702018, and 51561145021), and the Youth Innovation Promotion Association, CAS. The authors also thank Cuiying Ye and Wenjie Yan for device fabrications and measurements.

Conflict of Interest

The authors declare no conflict of interest.

Data Availability Statement

The data that support the findings of this study are available from the corresponding author upon reasonable request.

Keywords

durability, electrical load capacity, energy harvesting, triboelectric nanogenerators, power density

Received: May 27, 2022

Revised: June 27, 2022

Published online:

- [1] a) S. Chu, A. Majumdar, *Nature* **2012**, *488*, 294; b) D. Butler, *Nature* **2006**, *440*, 402; c) R. K. Jain, J. Qin, R. Rajagopal, *Nat. Energy* **2017**, *2*, 17112; d) H. S. Boudet, *Nat. Energy* **2019**, *4*, 446.
- [2] a) J. Kim, A. S. Campbell, B. E.-F. de Ávila, J. Wang, *Nat. Biotechnol.* **2019**, *37*, 389; b) L. Yin, K. N. Kim, J. Lv, F. Tehrani, M. Lin, Z. Lin, J. M. Moon, J. Ma, J. Yu, S. Xu, J. Wang, *Nat. Commun.* **2021**, *12*, 1542; c) Z. L. Wang, *Nano Energy* **2019**, *58*, 669.
- [3] a) X. Zhao, H. Askari, J. Chen, *Joule* **2021**, *5*, 1391; b) W. Xu, H. Zheng, Y. Liu, X. Zhou, C. Zhang, Y. Song, X. Deng, M. Leung, Z. Yang, R. X. Xu, Z. L. Wang, X. C. Zeng, Z. Wang, *Nature* **2020**, *578*, 392; c) R. Cheng, K. Dong, P. Chen, C. Ning, X. Peng, Y. Zhang, D. Liu, Z. L. Wang, *Energy Environ. Sci.* **2021**, *14*, 2460.
- [4] a) Z. L. Wang, *Nano Energy* **2020**, *68*, 104272; b) Z. L. Wang, *Mater. Today* **2017**, *20*, 74; c) X. Xiao, X. Zhang, S. Wang, H. Ouyang, P. Chen, L. Song, H. Yuan, Y. Ji, P. Wang, Z. Li, M. Xu, Z. L. Wang, *Adv. Energy Mater.* **2019**, *9*, 1902460.
- [5] a) P. F. Chen, J. An, R. Cheng, S. Shu, A. Berbille, T. Jiang, Z. L. Wang, *Energy Environ. Sci.* **2021**, *14*, 4523; b) C. Rodrigues, D. Nunes, D. Clemente, N. Mathias, J. M. Correia, P. Rosa-Santos, F. Taveira-Pinto, T. Morais, A. M. Pereira, J. Ventura, *Energy Environ. Sci.* **2020**, *13*, 2657; c) C. Shan, W. He, H. Wu, S. Fu, Q. Tang, Z. Wang, Y. Du, J. Wang, H. Guo, C. Hu, *Adv. Energy Mater.* **2022**, *12*, 2200963.
- [6] a) J. Chen, Y. Huang, N. Zhang, H. Zou, R. Liu, C. Tao, X. Fan, Z. L. Wang, *Nat. Energy* **2016**, *1*, 16138; b) R. Cheng, K. Dong, L. Liu, C. Ning, P. Chen, X. Peng, D. Liu, Z. L. Wang, *ACS Nano* **2020**, *14*, 15853.
- [7] R. Hinchet, H.-J. Yoon, H. Ryu, M.-K. Kim, E.-K. Choi, D.-S. Kim, S.-W. Kim, *Science* **2019**, *365*, 491.
- [8] a) H. Guo, J. Chen, L. Wang, A. C. Wang, Y. Li, C. An, J.-H. He, C. Hu, V. K. S. Hsiao, Z. L. Wang, *Nat. Sustain.* **2020**, *4*, 147; b) A. Li, Y. Zi, H. Guo, Z. L. Wang, F. M. Fernandez, *Nat. Nanotechnol.* **2017**, *12*, 481.
- [9] a) H. Wang, L. Xu, Y. Bai, Z. L. Wang, *Nat. Commun.* **2020**, *11*, 4203; b) Z. L. Wang, *Nature* **2017**, *542*, 159; c) H. Wang, C. Zhu, W. Wang, R. Xu, P. Chen, T. Du, T. Xue, Z. Wang, M. Xu, *Nanomaterials* **2022**, *12*, 594.

- [10] Z. L. Wang, *Rep. Prog. Phys.* **2021**, *84*, 096502.
- [11] a) Y. Xie, S. Wang, S. Niu, L. Lin, Q. Jing, J. Yang, Z. Wu, Z. L. Wang, *Adv. Mater.* **2014**, *26*, 6599; b) J. An, P. Chen, Z. Wang, A. Berbille, H. Pang, Y. Jiang, T. Jiang, Z. L. Wang, *Adv. Mater.* **2021**, *33*, 2101891.
- [12] H. Fu, X. Mei, D. Yurchenko, S. Zhou, S. Theodossiades, K. Nakano, E. M. Yeatman, *Joule* **2021**, *5*, 1074.
- [13] Z. Yang, Y. Yang, H. Wang, F. Liu, Y. Lu, L. Ji, Z. L. Wang, J. Cheng, *Adv. Energy Mater.* **2021**, *11*, 2101147.
- [14] W. He, W. Liu, J. Chen, Z. Wang, Y. Liu, X. Pu, H. Yang, Q. Tang, H. Yang, H. Guo, C. Hu, *Nat. Commun.* **2020**, *11*, 4277.
- [15] Z. Zhao, Y. Dai, D. Liu, L. Zhou, S. Li, Z. L. Wang, J. Wang, *Nat. Commun.* **2020**, *11*, 6186.
- [16] X. Fu, S. Xu, Y. Gao, X. Zhang, G. Liu, H. Zhou, Y. Lv, C. Zhang, Z. L. Wang, *ACS Energy Lett.* **2021**, *6*, 2343.
- [17] a) P. F. Chen, J. An, S. Shu, R. Cheng, J. Nie, T. Jiang, Z. L. Wang, *Adv. Energy Mater.* **2021**, *11*, 2003066; b) J. Han, Y. Feng, P. Chen, X. Liang, H. Pang, T. Jiang, Z. L. Wang, *Adv. Funct. Mater.* **2021**, *32*, 2108580.
- [18] J. Chen, H. Guo, C. Hu, Z. L. Wang, *Adv. Energy Mater.* **2020**, *10*, 2000886.
- [19] a) H. Pang, Y. Feng, J. An, P. Chen, J. Han, T. Jiang, Z. L. Wang, *Adv. Funct. Mater.* **2021**, *31*, 2106398; b) Y. Feng, J. Han, M. Xu, X. Liang, T. Jiang, H. Li, Z. L. Wang, *Adv. Energy Mater.* **2022**, *12*, 2103143.
- [20] L. Long, W. Liu, Z. Wang, W. He, G. Li, Q. Tang, H. Guo, X. Pu, Y. Liu, C. Hu, *Nat. Commun.* **2021**, *12*, 4689.
- [21] Y. Liu, W. Liu, Z. Wang, W. He, Q. Tang, Y. Xi, X. Wang, H. Guo, C. Hu, *Nat. Commun.* **2020**, *11*, 1599.
- [22] S. Niu, Y. Liu, S. Wang, L. Lin, Y. S. Zhou, Y. Hu, Z. L. Wang, *Adv. Mater.* **2013**, *25*, 6184.
- [23] a) S. Wang, Y. Xie, S. Niu, L. Lin, Z. L. Wang, *Adv. Mater.* **2014**, *26*, 2818; b) S. Niu, Z. L. Wang, *Nano Energy* **2015**, *14*, 161.
- [24] a) W. Yan, Y. Liu, P. Chen, L. N. Y. Cao, J. An, T. Jiang, W. Tang, B. Chen, Z. L. Wang, *Adv. Energy Mater.* **2022**, *12*, 2103677; b) Z. Wang, W. Liu, W. He, H. Guo, L. Long, Y. Xi, X. Wang, A. Liu, C. Hu, *Joule* **2021**, *5*, 441.